

MOLECULAR GAS TOWARD SUPERNOVA REMNANT CASSIOPEIA A

PING ZHOU,^{1,2} JIANG-TAO LI,³ ZHI-YU ZHANG,^{4,5} JACCO VINK,^{1,6,7} YANG CHEN,^{2,8} MARIA ARIAS,¹ DANIEL PATNAUDE,⁹
AND JOEL N. BREGMAN³

¹*Anton Pannekoek Institute for Astronomy, University of Amsterdam, Science Park 904, 1098 XH Amsterdam, The Netherlands*

²*School of Astronomy and Space Science, Nanjing University, 163 Xianlin Avenue, Nanjing, 210023, China*

³*Department of Astronomy, University of Michigan, 311 West Hall, 1085 S. University Ave, Ann Arbor, MI, 48109-1107, U.S.A.*

⁴*Institute for Astronomy, University of Edinburgh, Royal Observatory, Blackford Hill, Edinburgh EH9 3HJ, UK*

⁵*ESO, Karl Schwarzschild Strasse 2, D-85748 Garching, Munich, Germany*

⁶*GRAPPA, University of Amsterdam, Science Park 904, 1098 XH Amsterdam, The Netherlands*

⁷*SRON, Netherlands Institute for Space Research, Sorbonnelaan 2, 3584 CA Utrecht, The Netherlands*

⁸*Key Laboratory of Modern Astronomy and Astrophysics, Nanjing University, Ministry of Education, China*

⁹*Smithsonian Astrophysical Observatory, Cambridge, MA 02138, USA*

(Accepted August 7, 2018)

Submitted to ApJ

ABSTRACT

We mapped ¹²CO $J=1-0$, ¹²CO $J=2-1$, ¹³CO $J=1-0$, and ¹³CO $J=2-1$ lines toward supernova remnant (SNR) Cassiopeia A with the IRAM 30m telescope. The molecular clouds (MCs) along the line of sight of Cas A do not show optically thin, shock-broadened ¹²CO lines ($\Delta V \leq 7 \text{ km s}^{-1}$ toward Cas A), or high-temperature features from shock heating ($T_k \leq 22 \text{ K}$ toward Cas A). Therefore, we suggest that there is no physical evidence to support that the SNR is impacting the molecular gas. All the detected MCs are likely in front of Cas A, as implied by the HCO⁺ absorption line detected in the same velocity ranges. These MCs contribute H₂ column densities of $5 \times 10^{21} \text{ cm}^{-2}$, $5 \times 10^{21} \text{ cm}^{-2}$, and $2 \times 10^{21} \text{ cm}^{-2}$ in the west, south, and center of the SNR, respectively. The 20 K warm gas at $V_{\text{LSR}} \sim -47 \text{ km s}^{-1}$ is distributed along a large-scale molecular ridge in the south of Cas A. Part of the gas is projected onto Cas A, providing a foreground H₂ mass of $\sim 200(d/3 \text{ kpc})^2 M_{\odot}$, consistent with the mass of cold dust (15–20 K; 2–4 M_{\odot}) found in front of the SNR. We suggest that the 20 K warm gas is heated by background cosmic rays with an ionization rate of $\zeta(\text{H}_2) \sim 2 \times 10^{-16} \text{ s}^{-1}$. The cosmic rays and X-ray emission from Cas A are excluded as the heating sources of the clouds.

Keywords: ISM: individual objects (Cas A)— ISM: supernova remnants — ISM: molecules — cosmic rays

1. INTRODUCTION

Cassiopeia A, a.k.a., Cas A (G111.7–2.1), is the remnant of a young supernova that exploded around AD 1681 ± 19 (Fesen et al. 2006) at a distance of $3.4_{-0.1}^{+0.3}$ kpc (Reed et al. 1995). Due to its youth and brightness, Cas A is among the best-observed supernova remnants (SNRs) and the prototype for many aspects of SNR studies. The current manifestations of an SNR are the combined results of the intrinsic supernova properties and the environment it evolves in. The study of the environment not only provides crucial information of the SNR itself, but also helps us to understand how supernova explosions affect the interstellar medium of the galaxies. In spite of a wealth of observations of Cas A across the electromagnetic wavelengths, there is no consensus on the immediate SNR environment.

It is a common view that Cas A evolves in the stellar winds of the progenitor star. The early suggestion of the idea was based on the detections of the quasi-stationary flocculi (van den Bergh et al. 1973). The circumstellar medium of Cas A was likely produced by slow and dense winds, characterized by a $\rho_w \propto r^{-2}$ density profile (e.g., Vink 2004). This picture well explains the positions of the SNR’s forward and reverse shocks (Chevalier & Oishi 2003), the X-ray properties of shocked ejecta knots (Laming & Hwang 2003; Hwang & Laming 2009), and the characteristics of the shocked ambient gas (Lee et al. 2014). The preshock density estimated from the X-ray analysis is around $0.9 \pm 0.3 \text{ cm}^{-3}$, without strong variation at different position angles (Lee et al. 2014).

Outside the SNR boundary the environmental gas is cooler and its relation with Cas A less clear. The difficulty is how to distinguish the immediate environment and the interstellar medium along the line of sight. The dense gas along the line of sight of Cas A is mainly distributed in the velocity range of -50 to -30 km s^{-1} (associated with the Perseus arm), and at $\sim 0 \text{ km s}^{-1}$ (associated the Orion spur), as observed in molecular emission and absorption lines (de Jager et al. 1978; Batrla et al. 1983, 1984; Goss et al. 1984; Bieging & Crutcher 1986; Wilson et al. 1993; Anantharamaiah et al. 1994; Reynoso & Goss 2002; Kilpatrick et al. 2014), H I absorption (Mebold & Hills 1975; Bieging et al. 1991; Schwarz et al. 1997), [C I] (Mookerjee et al. 2006), and carbon recombination lines (Payne et al. 1989; Anantharamaiah et al. 1994; Kantharia et al. 1998; Mookerjee et al. 2006; Oonk et al. 2017; Salas et al. 2017, 2018). Reynoso et al. (1997) found some small absorption H I features at the lower LSR velocity of -69 to -62 km s^{-1} , and suggested that they are from neutral knots driven away by the pro-

genitor wind of Cas A. If this velocity of foreground H I structures represents the upper limit of Cas A’s systemic velocity, it may indicate that Cas A is not associated with any of the clouds in the velocity range of -50 to -30 km s^{-1} . This idea is supported by the carbon recombination line studies, which suggest that the gas at $V_{\text{LSR}} \lesssim -47 \text{ km s}^{-1}$ is at least 100 pc in front of Cas A (Kantharia et al. 1998; Salas et al. 2017). However, since the molecular gas is traced by molecular lines, the relationship between the molecular gas and Cas A should be studied with molecular observations.

Warm molecular gas with a kinetic temperature of 20 K was found at $V_{\text{LSR}} \sim -47 \text{ km s}^{-1}$ (Wilson et al. 1993), using ^{13}CO and ^{12}CO observations with IRAM 30 m, while the typical temperature of an interstellar giant molecular cloud (MC) is ~ 10 K. The association between Cas A and molecular clouds (MCs) was proposed in a recent study using the SMT 12 m telescope (Kilpatrick et al. 2014), based on a subtle line broadening (line width of $\sim 6 \text{ km s}^{-1}$) of the ^{12}CO emission at $V_{\text{LSR}} \sim -37 \text{ km s}^{-1}$ and $\sim -47 \text{ km s}^{-1}$ in the west and south of the SNR. If true, the MCs could provide dense targets for the shock and cosmic-ray (CR) protons to interact, making the properties of the MCs important constraints for the studies of the SNR’s shock and CRs. However, an association between Cas A and MC is inconsistent with the low preshock density found in X-rays (Lee et al. 2014) and the suggestion that the clouds at $V_{\text{LSR}} = -50$ – 0 km s^{-1} are all foreground gas.

Motivated by the aforementioned problems, we performed new molecular line observations toward Cas A and its environment, aiming to answer the following questions: Is the SNR interacting with MCs? what are the properties of the MCs? We also examine what is the heating source of the 20 K MC at -47 km s^{-1} . Our molecular mapping observations have the best angular resolution of these lines to date for this SNR ($11''$ at $^{12}\text{CO } J=2-1$), and good sky coverage (83 arcmin^2 at $^{12}\text{CO } J=2-1$).

2. DATA

2.1. IRAM 30 m observation

We performed 3 and 1 mm heterodyne observations toward Cas A with the IRAM 30 m telescope, during 2016 July 12, September 24, November 15–19, and December 5 (Project IDs 145-15, 053-16, and 136-16; PI: Jiang-Tao Li), and 2017 September 16–18 (029-17; PI: Ping Zhou). The observations consist of mappings of the SNR and line surveys of a few positions of interest. This work focuses on the ^{12}CO and ^{13}CO mapping observations, but also uses the HCO^+ observation at one position.

Table 1. Observational information

Line	Frequency (GHz)	Instrument	HPBW (arcsec)	Map Area (arcmin ²)	Average/Central rms ^a (K)
¹² CO $J=2-1$	230.540	HERA+EMIR	10.7	83	0.65/0.29
¹³ CO $J=2-1$	220.399	HERA+EMIR	11.2	54	0.30/0.21
¹² CO $J=1-0$	115.271	EMIR	21.3	79	0.27/0.22
¹³ CO $J=1-0$	110.201	EMIR	22.3	69	0.12/0.09
HCO ⁺ $J=1-0$	89.188	EMIR	27.6	-	0.008

^aThe rms of the spectrum in each pixel ($\approx 1/2$ of the HPBW) with a velocity resolution of 0.5 km s^{-1} in the velocity range from -100 km s^{-1} to 50 km s^{-1} . The central rms is calculated from the interior $7' \times 7'$ region centered at ($23^{\text{h}}23^{\text{m}}27^{\text{s}}$, $58^{\circ}48'40''$, J2000), where deeper observations were taken.

We mapped ¹²CO $J=1-0$ (at 115.271 GHz), ¹³CO $J=1-0$ (at 110.201 GHz), ¹²CO $J=2-1$ (at 230.540 GHz) and ¹³CO $J=2-1$ (at 220.399 GHz) emission toward Cas A and its vicinity, using the on-the-fly mode with the 9-pixel dual-polarization HETerodyne Receiver Array (HERA) and the Eight MIXer Receiver (EMIR). On 2016 July 12 and September 24, the HERA was used to map the ¹²CO $J=2-1$ and ¹³CO $J=2-1$ lines. The back end of fast Fourier transform spectrometers (FTSs) provided a frequency resolution of 50 kHz, corresponding to a velocity resolution of 0.063 km s^{-1} . Bad spectra produced by problematic pixels of HERA were removed. For the rest of the mapping observation, we used EMIR to observe the ¹²CO and ¹³CO lines at 1 and 3 mm bands, simultaneously. In the EMIR observations FTSs were tuned to the 200 kHz resolution, which provided a velocity resolution of 0.25 km s^{-1} for the ¹²CO $J=2-1$ line and 0.5 km s^{-1} for the ¹²CO $J=1-0$ line. Although we optimized the observations for the velocity range of $V_{\text{LSR}} = -100-50 \text{ km s}^{-1}$, the FTS units covered a wide frequency range of 8 GHz at 200 kHz resolution, corresponding to a velocity coverage of $\sim 10^4 \text{ km s}^{-1}$ for the ¹²CO $J=2-1$ line and $\sim 2 \times 10^4 \text{ km s}^{-1}$ for the ¹²CO $J=1-0$ line. By inspecting the spectra in the wide velocity range, we only found strong emission lines at the velocity range from $V_{\text{LSR}} \sim -50 \text{ km s}^{-1}$ to $V_{\text{LSR}} \sim 0 \text{ km s}^{-1}$. Given that we aim to study the interstellar MCs, we only provide detailed analysis of the data in the velocity range from -100 to 50 km s^{-1} , where the baselines were reduced with linear lines. We do not show the results of the wide velocity range, also because the baselines of the very wide band are not linear or stable in different observational epochs, but sometimes contaminated by instrumental features and

large noises at some velocities. The half-power beam width (HPBW) of the telescope was $10''.7$ at 230 GHz and $21''.3$ at 115 GHz. The main-beam efficiencies at these two frequencies were 59% and 78%, respectively.

We also carried out a 1 mm line survey toward a few positions in and near Cas A, using the positional switch mode. As this paper focuses on the relation of Cas A to its environment, we only use one spectrum of HCO⁺ $J=1-0$ at the western radio peak ($23^{\text{h}}23^{\text{m}}10^{\text{s}}$, $58^{\circ}48'40''$, J2000), where absorption lines are seen and will provide clues to the location of MCs. The rest of the survey data will be analyzed in another paper. The back-end FTS was working at the frequency resolution of 50 kHz, providing a velocity resolution of 0.17 km s^{-1} at a frequency of 89.188 GHz. The beam efficiency was 81 % at this frequency.

The detailed observation information used in this work is tabulated in Table 1. The IRAM 30m data were reduced with the GILDAS software¹.

2.2. FCRAO archival data

We retrieve large-scale mapping data of ¹²CO $J=1-0$ produced by the Canadian Galactic Plane Survey (CGPS). The original data are from “The Five College Radio Astronomy Observatory (FCRAO) CO Survey of the Outer Galaxy” (Heyer et al. 1998). The data have been regridded from the FCRAO $50''.22$ pixel scale to the CGPS $18''$ pixel scale, with a velocity step of 0.82 km s^{-1} . Prior to spatial regridding the data were smoothed to the Nyquist resolution limit of $1''.674$. A main-beam efficiency of 0.48 is adopted.

¹ <http://www.iram.fr/IRAMFR/GILDAS/>

3. RESULTS

3.1. Distribution of the MCs

The ^{13}CO and ^{12}CO emission is shown at the local standard of rest velocities $V_{\text{LSR}} = -50$ to -30 km s^{-1} , and -2 km s^{-1} , respectively, as indicated by spectra averaged in the field of view (FOV; see the top-left panels of Figure 1 and 2). We only analyze the molecular gas at the velocity range between -50 km s^{-1} and -30 km s^{-1} , since the gas at $V_{\text{LSR}} \sim 0 \text{ km s}^{-1}$ corresponds to a local component (Dame et al. 2001) that is unrelated to the remnant.

The distribution of MC column density can be described with the ^{13}CO $J=1-0$ map, quiescent molecular gas, given that ^{13}CO emission is found to be optically thin ($\tau_{^{13}\text{CO}} < 1$) for the MCs toward Cas A. Figure 1 shows the ^{13}CO distribution at different velocities. The molecular gas is mainly distributed in the south ($V_{\text{LSR}} = -47 \text{ km s}^{-1}$) and west ($V_{\text{LSR}} = -41$ to -35 km s^{-1}), with some clouds projected onto the SNR. The north of the SNR does not show any MC emission, as also the ^{13}CO $J=2-1$ data show a similar distribution to the ^{13}CO $J=1-0$ data.

The ^{12}CO $J=2-1$ channel images reveal more extended structures from both high and low column density parts of the MCs (see Figure 2). At -47 km s^{-1} , some bright filamentary structures are shown near the SNR, which are not clearly shown in other velocity channels, indicating a small velocity dispersion of these structures. The western clouds are fainter but span a larger velocity range of -41 km s^{-1} to -35 km s^{-1} . Although the northern part of SNR shows very little molecular gas, there is a faint, thin filament outside the SNR north-eastern boundary (-37 km s^{-1}) and a small cloud to the north (-41 km s^{-1}).

3.2. Temperatures of the MCs

The measured main-beam temperature of the CO emission is determined by the excitation temperature T_{ex} , optical depth τ , and beam filling factor f ($f < 1$ if the clumpy gas is unresolved with the telescope's beam):

$$T_{\text{mb}} = f \frac{h\nu}{k} \left(\frac{1}{e^{h\nu/kT_{\text{ex}}} - 1} - \frac{1}{e^{h\nu/kT_{\text{bg}}} - 1} \right) (1 - e^{-\tau}), \quad (1)$$

where the background temperature $T_{\text{bg}} = 2.73 \text{ K}$ and ν is the line frequency.

We assume that the ^{12}CO $J=1-0$ emission is optically thick, with $\tau_{^{12}\text{CO}} \gg 1$, which is a valid approximation for MCs with H_2 column density $N(\text{H}_2) \gtrsim 10^{21} \text{ cm}^{-2}$ (see discussion in Section 4.2). Under the assumption of local thermodynamic equilibrium (LTE), the excitation temperatures of different lines are the same and are

equal to the kinetic temperature of the molecular gas T_{k} . We obtain the kinetic temperature T_{k} ($= T_{\text{ex}}$ in LTE) with the main-beam temperature of the ^{12}CO $J=1-0$ emission:

$$T_{\text{k}} = \frac{5.53}{\ln\{1 + 5.53/[T_{\text{mb}}(^{12}\text{CO})/f + 0.84]\}} \text{ K}. \quad (2)$$

The gas temperature is thus inferred by the optically thick ^{12}CO $J=1-0$ line with given f . Figure 3 shows T_{k} of the MCs at two velocity intervals of -50 to -44 km s^{-1} and -44 to -30 km s^{-1} . The latter velocity range is large and covers a few gas components (see Figure 2). If multiple line components exist along the line of sight, the T_{k} is derived from the component with the highest T_{mb} . The T_{k} in each pixel is derived from $T_{\text{mb}}(^{12}\text{CO})$ at the given velocity range with an assumed beam filling factor $f = 1$. Note that the assumptions of $f = 1$ and $\tau_{^{12}\text{CO}} \gg 1$ are not valid at the outer layers of MCs, where T_{mb} is smaller owing to the clumpiness of the gas and small optical depth. Therefore, the gas temperature at each velocity interval is best represented by the inner part of the clouds, where $f \approx 1$ and T_{k} appears to be the highest.

Notably, the MC at -50 to -44 km s^{-1} has a significantly higher temperature ($\sim 20 \text{ K}$) than all those in the velocity range of -44 to -30 km s^{-1} ($\sim 13 \text{ K}$, typical in interstellar MCs), implying that an extra heating source is needed to warm the cloud. The 20 K warm gas is distributed both inside Cas A (projected) and far outside the SNR, which does not support the SNR shock being the direct heating source of the warm gas, otherwise, we would only find hotter gas at/inside the SNR boundary.

3.3. Molecular line profiles

Physical interaction between SNR and MC involves heating and perturbation of the MCs by the SNR shock. The observational manifestations of the SNR-MC interaction in molecular lines include the presence of broadened, optically thin lines with enhanced high- J to low- J ratios of molecular lines due to a high excitation (e.g., ^{12}CO $J=2-1/J=1-0$ ratio $R_{12/10} \approx 4 \exp(-11.1/T_{\text{k}}) > 1$), etc. See Jiang et al. (2010) and references therein for the SNRs showing these properties. The heated clouds are found to have temperatures from tens of kelvin in the low-velocity C-type shock (e.g., van Dishoeck et al. 1993) to hundreds of kelvin in the high-velocity J-type shock (Rho et al. 2015).

To find out whether the MCs are perturbed or heated by Cas A, we examine the line profiles of ^{12}CO $J=2-1$, ^{12}CO $J=1-0$, and ^{13}CO $J=1-0$ in three groups of regions: (1) near the boundary of Cas A, where the

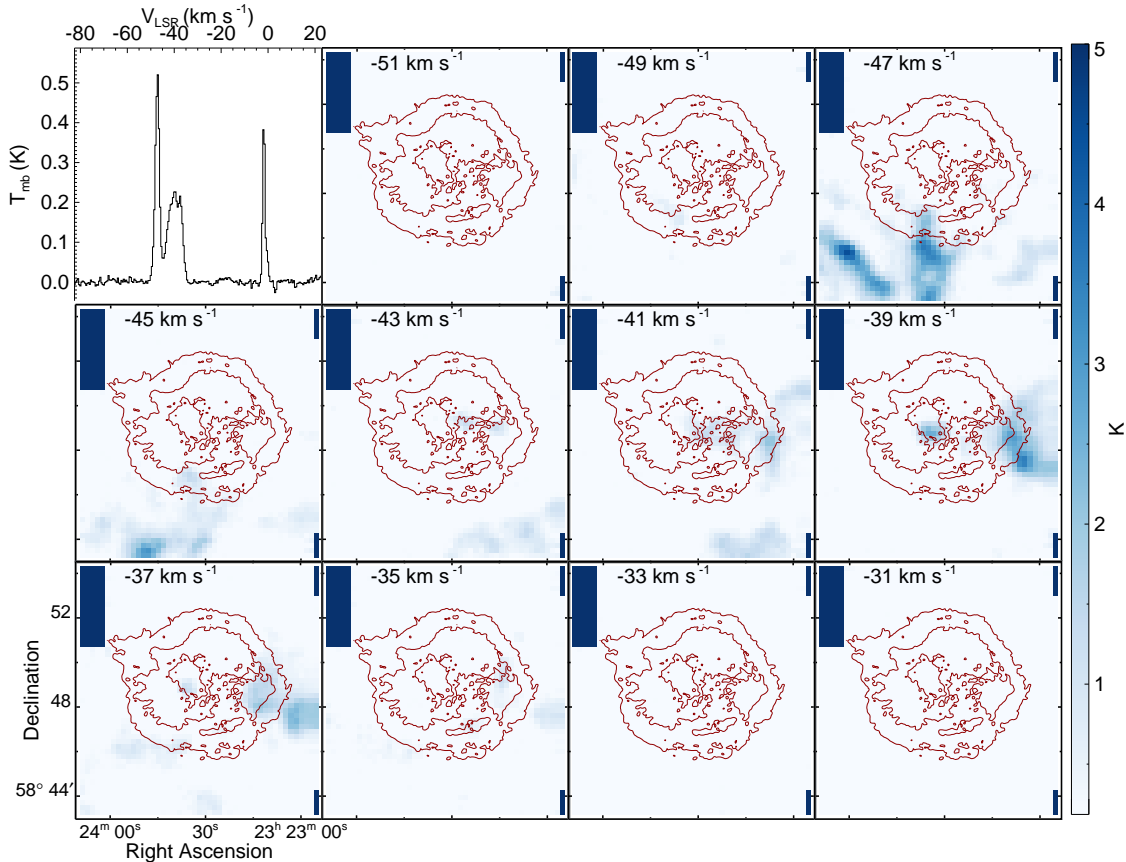


Figure 1. Channel map of the main-beam temperature of $^{13}\text{CO } J=1-0$ emission, overlaid with contours of *Chandra* X-ray emission. The same contours are used for the maps in the rest of the paper. The map size is $0^{\circ}.14 \times 0^{\circ}.15$, with a pixel size of $11''$. The top-left panel shows the spectrum averaged over the FOV. The corners in saturated blue color were not covered by the observation.

SNR–MC interaction might occur; (2) at the CO T_{mb} peaks (search for line broadenings due to shocks); and (3) where slightly broad CO line widths ($> 6 \text{ km s}^{-1}$) were found by Kilpatrick et al. (2014). The regions are labeled in Figure 3 with cyan boxes, blue dashed boxes ($33'' \times 33''$), and red plus signs, respectively. The $^{12}\text{CO } J=2-1$ datacube used here is convolved to the beam size of the $^{12}\text{CO } J=1-0$ datacube. We search for broadened lines with FWHM ΔV significantly larger than that of the environmental gas. The ^{12}CO emission from the shocked gas is expected to be optically thin, characterized by larger $^{12}\text{CO}/^{13}\text{CO}$ line ratio (close to an abundance ratio of ^{12}CO to ^{13}CO of ~ 60 ; Lucas & Liszt 1998). The shocked MCs should also be heated to higher temperatures, with $R_{21/10} > 1$ and T_{mb} that differ from those in the preshock regions. Note that the 20 K warm clouds outside the SNR also show $R_{21/10} > 1$ at the optically thin case, but given their location, they cannot be heated by the SNR shock. We must take the line widths into account, so as to distinguish the SNR-shocked gas and the gas with other extra heating.

First, we extract lines from the edge of Cas A (denoted by odd numbers), and compare them with those from nearby “preshock” regions (denoted by even numbers; see regions in Figure 3 and line profiles in Figure 4). There are two main line components ($\sim -47 \text{ km s}^{-1}$ and $\sim -37 \text{ km s}^{-1}$) in a small velocity range (-50 to -30 km s^{-1}), each with a velocity width of a few km s^{-1} . None of the lines show $\Delta V \gtrsim 10 \text{ km s}^{-1}$, which is expected for shocked gas that has higher velocity dispersion than the environmental gas with ΔV up to $6-7 \text{ km s}^{-1}$ (regions 24, 26, 28). Moreover, the line profiles at the SNR edge are not broader than those from “preshock” regions. A few regions (5, 7, 13, and 17) show narrow redshift ^{12}CO wings of the $V_{\text{LSR}} = -47 \text{ km s}^{-1}$ component, which are indistinguishable from profiles of interstellar MCs that have line crowding along the line of sight (check external regions 16 and 18). Although in some regions (2, 3, 5, 6) the $R_{21/10}$ is marginally larger than 1 at $V_{\text{LSR}} \sim 47 \text{ km s}^{-1}$, the line widths of about 2 km s^{-1} are too narrow to be considered shocked features. In western regions

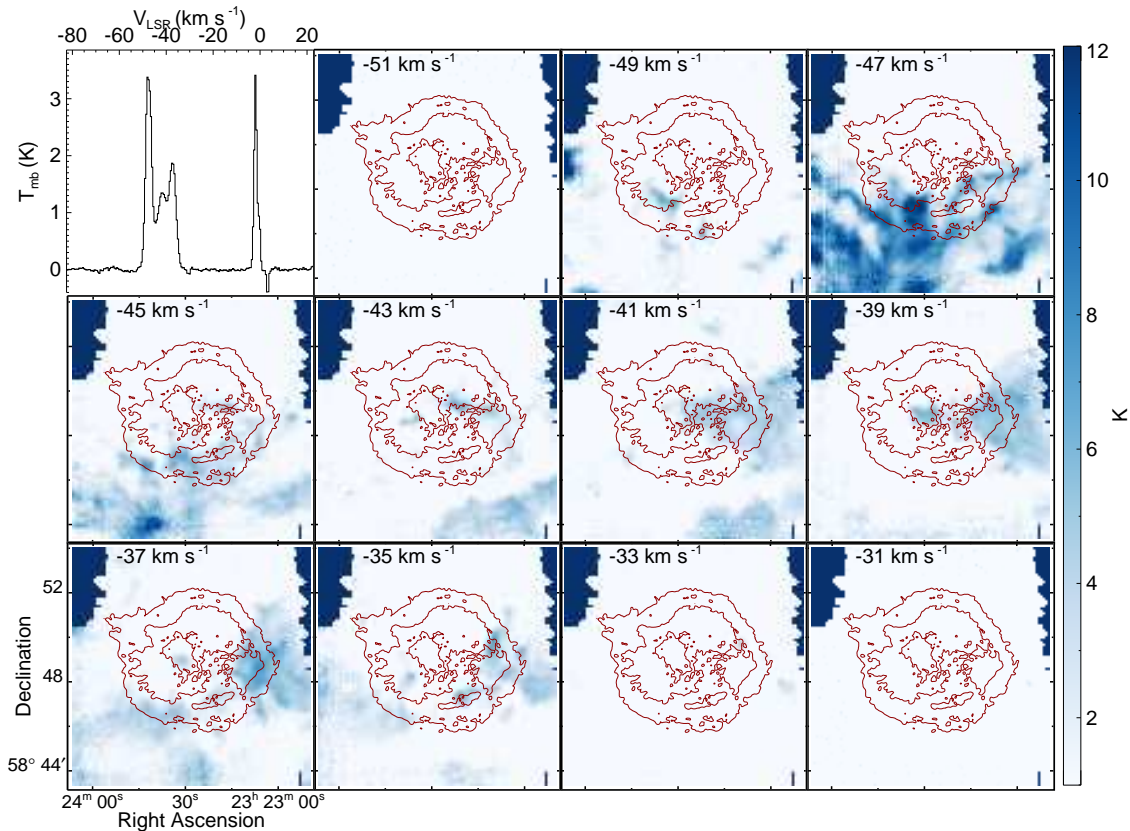


Figure 2. Channel maps of the main-beam temperature of $^{12}\text{CO } J=2-1$. The map size is $0^{\circ}15 \times 0^{\circ}15$, with a pixel size of $5''.5$. The top-left panel shows the spectrum averaged over the FOV.

23–28, the ^{13}CO emission has $\Delta V \sim 3-4 \text{ km s}^{-1}$ at $V_{\text{LSR}} \sim -39 \text{ km s}^{-1}$. Despite the slightly larger line widths ($\sim 6 \text{ km s}^{-1}$), the ^{12}CO lines reveal flatter tops, indicating that the ^{12}CO profiles could be affected by the opacity broadening (Phillips et al. 1979; Hacar et al. 2016). Moreover, given that the ^{12}CO emission is optically thick and has a small $T_{\text{mb}} (\lesssim 10 \text{ K})$, the western MCs consist of cold gas that has not been heated by the shock. Therefore, the line profiles in these regions do not reveal evidence of shock–MC interaction.

Second, some clouds at $V_{\text{LSR}} \sim -47 \text{ km s}^{-1}$ show strong ^{12}CO emission ($T_{\text{mb}} \gtrsim 15 \text{ K}$; regions are labeled in Figure 3). As shown in the fourth column of Figure 4, the ^{12}CO and ^{13}CO lines at $\sim -47 \text{ km s}^{-1}$ are narrow and optically thick, which are properties of quiescent molecular gas. The reason for the high $T_{\text{mb}}(^{12}\text{CO})$ for these regions is that they are at the interior parts of the MCs, with $\tau_{^{12}\text{CO}} \gg 1$ and filling factor $f \approx 1$ (see Equation (1)).

Finally, we show the line profiles of four regions (A–D), where the broad $^{12}\text{CO } J=2-1$ line width $\Delta v > 6 \text{ km s}^{-1}$ was suggested to be due to the SNR shock (Kilpatrick et al. 2014). We checked the ^{12}CO lines and

compared them with the ^{13}CO lines (see also our Figure 3). The $^{12}\text{CO } J=2-1$ lines from regions A–C reveal similar profiles to those in Kilpatrick et al. (2014, see their Figure 5), except that we found that the emission is twice as strong. The ^{12}CO line at region D shows a stronger line at -47 km s^{-1} , which could be a result of the better angular resolution of IRAM 30 m data compared to the previous SMT data for resolving the small molecular clumps. By comparing the three lines, we notice that all regions have $R_{21/10} \leq 1$, and the slightly “broad” ^{12}CO lines in clouds A, B, and D are clearly optically thick. For the same reasons that we stated for regions 23–28, there is no strong evidence for shock–MC interactions in regions A–D as well.

3.4. Clumps decomposed from the MCs

The MCs are clumpy (see Figure 2) and the ^{12}CO lines are found to be crowded in some regions. Instead of showing the spectra of each pixel, we decompose the MCs into multiple disjoint clump components, each associated with a single significant ^{12}CO emission peak. This would allow us to find whether there are any hot CO clumps with high intensity and CO lines with broad widths.

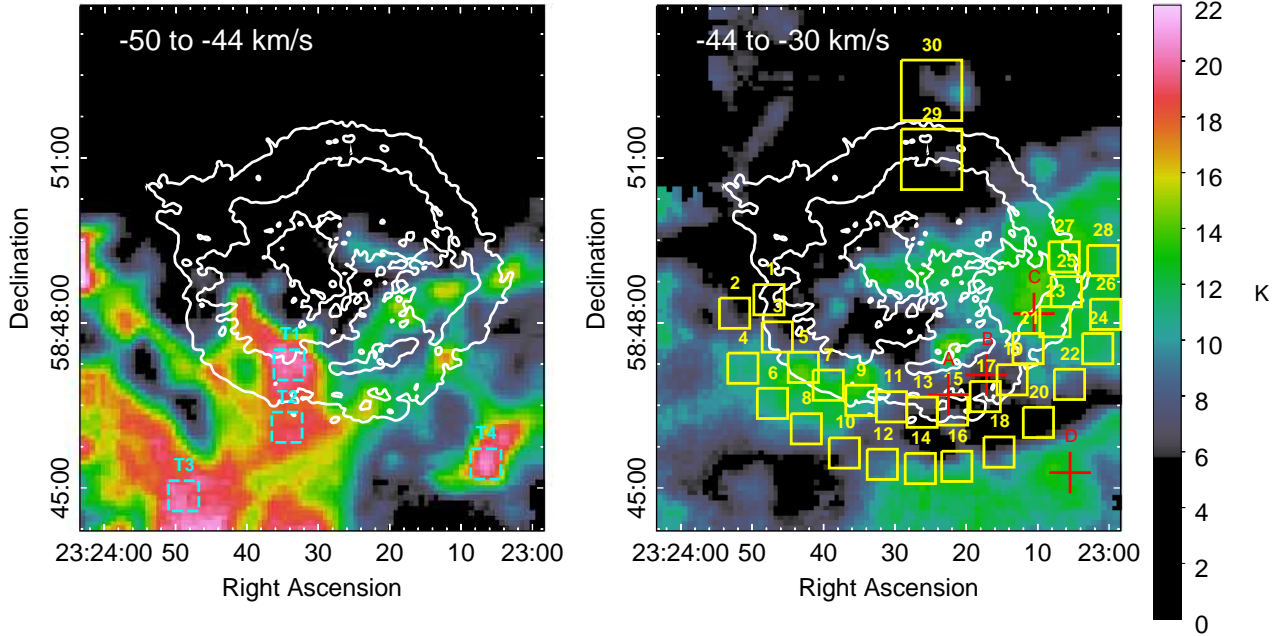


Figure 3. Kinetic temperature T_k maps of the molecular gas at velocities of -50 to -44 km s^{-1} and -44 to -30 km s^{-1} , respectively, assuming no beam dilution ($f = 1$) and $\tau_{12\text{CO}} \gg 1$. The real gas temperature is best represented by the high-temperature parts that are located in the MC interior, where the assumptions of $f = 1$ and $\tau_{12\text{CO}} \gg 1$ are valid. ^{12}CO and ^{13}CO spectra of the regions labeled with the boxes and plus signs are shown in Figure 4.

Using the ^{12}CO $J=2-1$ datacube in $V_{\text{LSR}} = -50$ to -30 km s^{-1} with a velocity resolution of 0.25 km s^{-1} , we identified 78 clumps in a $7' \times 7'$ region centered at ($23^{\text{h}}23^{\text{m}}27^{\text{s}}$, $58^{\circ}48'40''$, J2000), by applying the Fell-Walker clumpfind algorithm (Berry 2015) in the STARLINK package². Figure 5 displays the regions of the clumps on the ^{12}CO $J=2-1$ images at different velocity ranges. Each image shows clumps with peak velocities within the same velocity range. The identification method and the information of the clumps are elaborated in the Appendix A and Table 3.

The ^{12}CO $J=2-1$ clumps have peak main-beam temperatures T_{mb}^p in the range $2.2 - 16.7$ K, velocity dispersions dv in the range $0.3-2.5$ km s^{-1} , and sizes from subparsec to 3 pc. Under a Gaussian assumption of the lines, the velocity widths ΔV of these clumps are about $0.7 - 6$ km s^{-1} ($\text{FWHM} = 2.355\sigma$). The real line profiles could deviate from Gaussian distribution for some of the clumps. However, the small velocity dispersions do not favor the existence of bright, broad CO lines, consistent with the results obtained from inspecting the line profiles (see Section 3.3).

3.5. Absorption line of HCO^+ at -50 to -33 km s^{-1}

We detected absorption lines of HCO^+ $J=1-0$ at around the radio peak in the west of Cas A ($23^{\text{h}}23^{\text{m}}10^{\text{s}}$,

$58^{\circ}48'40''$, J2000; see spectrum in Figure 6). The absorption line at -50 to -33 km s^{-1} suggests that the background radio brightness exceeds the excitation temperature of HCO^+ , and that the HCO^+ gas at this velocity range is foreground gas.

The column density of HCO^+ can be obtained using the absorption the spectrum and the given the brightness of the continuum. The brightness temperature of the SNR's synchrotron emission at the radio peak is 1.85 K at the frequency of HCO^+ $J=1-0$. It is derived using the brightness temperature of 4.07 K at 32 GHz (observed with Effelsberg; Kraus et al. in prep) and a spectral index of -0.77 (Baars et al. 1977). The brightness temperature of the continuum is thus $T_{\text{cont}} \approx 4.6$ K after adding the contribution of the cosmic microwave background with $T_{\text{CMB}} = 2.73$ K. The column density of HCO^+ is given by (Godard et al. 2010)

$$N(\text{HCO}^+) = \frac{8.7 \times 10^{11} \int \tau(v) dv}{1 - \exp(-h\nu/kT_{\text{ex}})} \text{ cm}^{-2} \quad (3)$$

where the frequency $\nu = 89.188$ GHz, the optical depth $\tau = -\ln[T_{\text{line}}/T_{\text{cont}}]$.

We use three Gaussian lines to fit the HCO^+ spectrum and show the fitted results in Table 2 (also see the Gaussian components in Figure 6). The lower limits of the $N(\text{HCO}^+)$ values are tabulated, assuming that HCO^+ is not collisionally excited, with an excitation temperature $T_{\text{ex}} = 2.73$ K. We obtain a total HCO^+ column

² <http://starlink.eao.hawaii.edu/starlink>

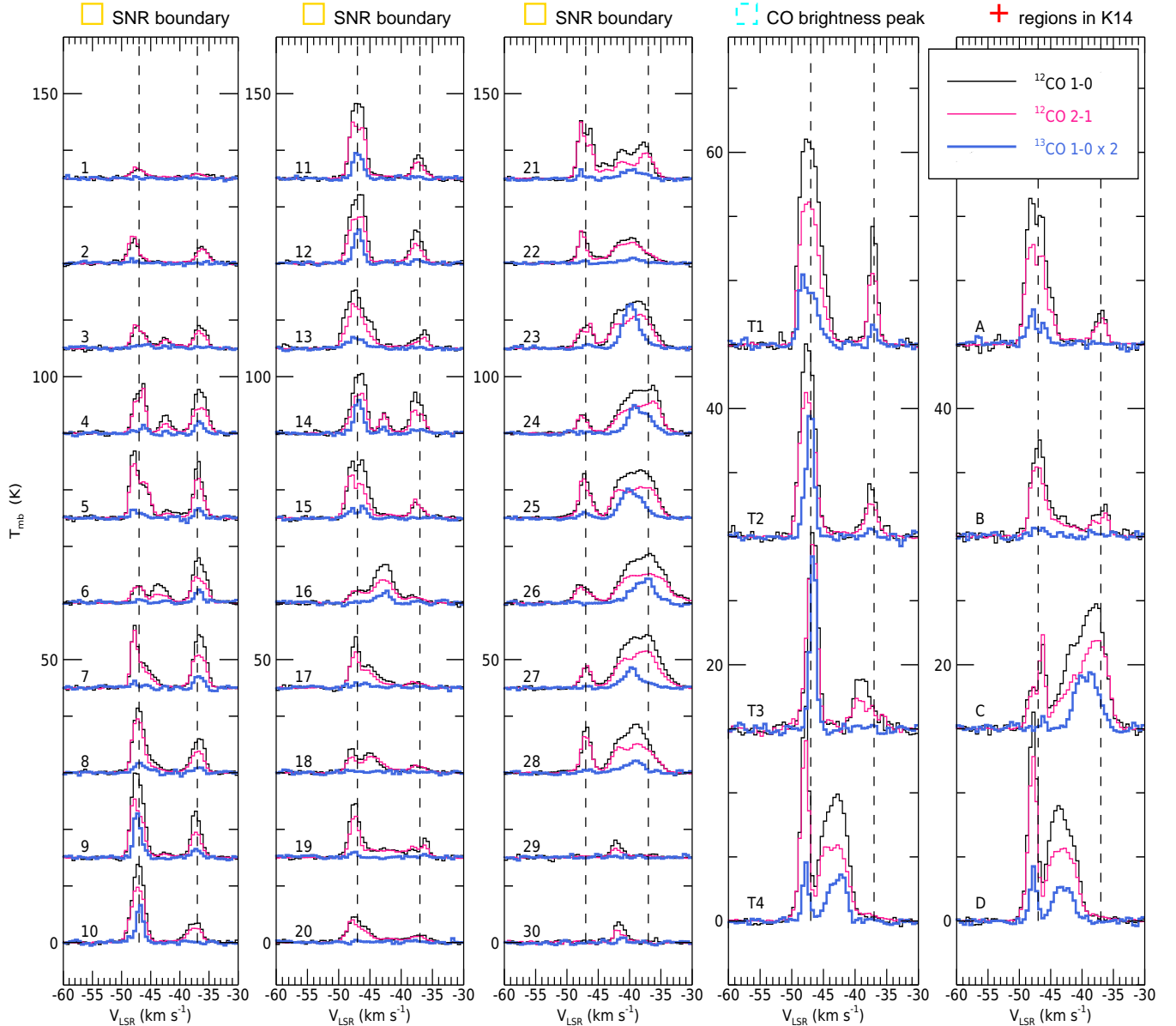


Figure 4. The $^{12}\text{CO } J=1-0$ (black line), $^{12}\text{CO } J=2-1$ (pink line), and $^{13}\text{CO } J=1-0$ (blue thick line) spectra extracted from the regions labeled in Figure 3. Three groups of regions are selected: regions near the SNR boundary labeled with numbers 1–30 (columns 1–3; odd and even numbers for regions inside and outside the SNR, respectively), ^{12}CO brightness peak labeled with T1–4 (column 4), and regions considered to have broad CO line width in Kilpatrick et al. (2014), labeled with A–D (column 5; spectra average from $\sim 50'' \times 50''$ boxes). The two vertical dashed lines indicate the velocities at -47 km s^{-1} and -37 km s^{-1} , respectively.

density of $5.7 \times 10^{11} \text{ cm}^{-2}$ in the velocity range -50 to -33 km s^{-1} .

4. DISCUSSION

4.1. Lack of evidence to support the SNR–MC interaction

According to our low- J ^{12}CO and ^{13}CO mapping of Cas A, the upper limits of the line width and temperature of the MCs are $\sim 7 \text{ km s}^{-1}$ and $\sim 22 \text{ K}$, respec-

tively. The MCs along the line of sight do not show any of the properties that are typical for shocked MCs: (1) optically thin broad line with FWHM much larger than that of the environmental gas (e.g. $> 10 \text{ km s}^{-1}$), (2) broadened CO lines accompanied by $R_{21/10} > 1$, and (3) MCs in post-shock regions much warmer than in the preshock regions. Therefore, we suggest that there is no physical evidence to support that the SNR is impacting the molecular gas. This is in accordance with the

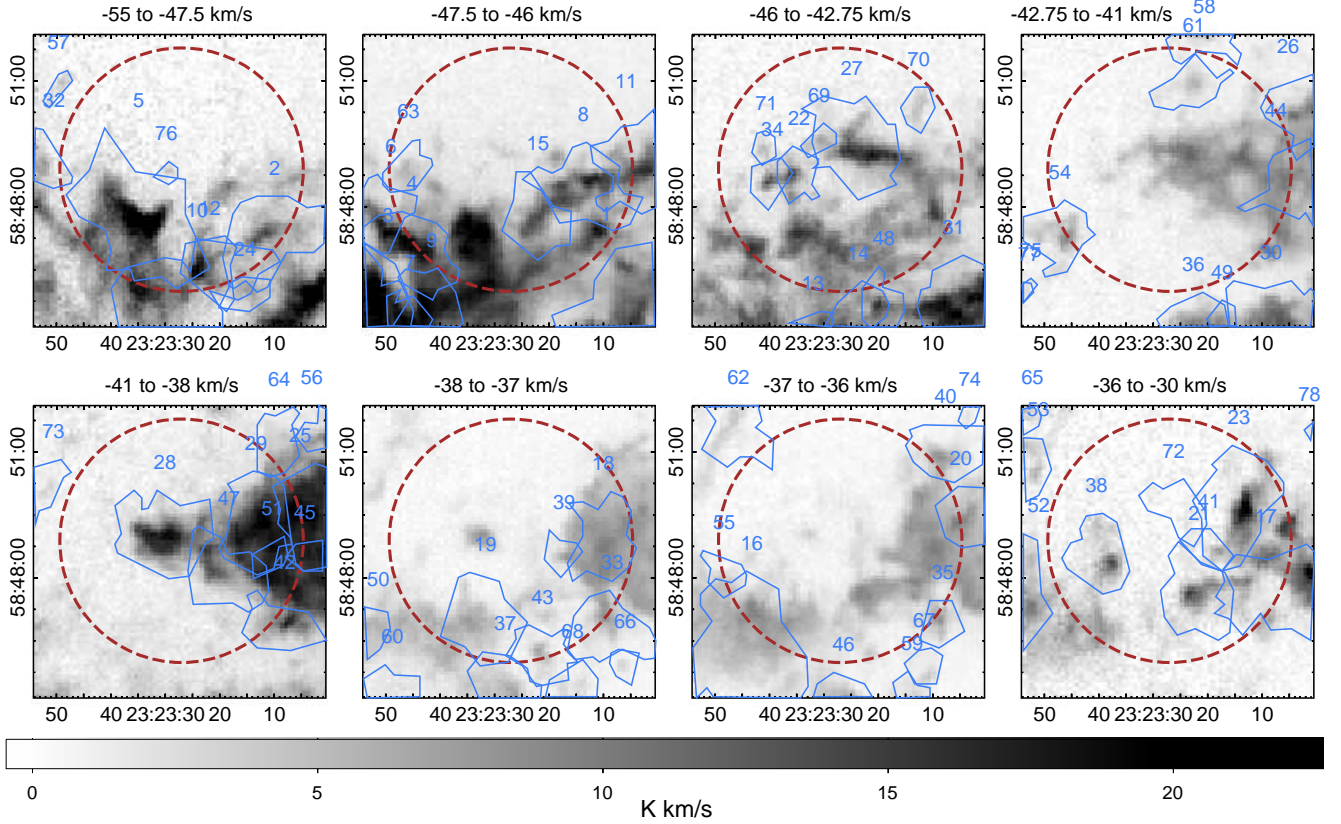


Figure 5. 78 identified clumps overlaid the $^{12}\text{CO } J=2-1$ images at eight different velocity ranges. The first panel shows 8 clumps with peak velocities within the velocity range labelled above, and for the rest panels each image shows 10 clumps. The polygon region is a fit to the outer boundary of the clump. The dashed circles indicate the the approximate shock front of the SNR (radius of 2.9). The detailed information of the clumps is tabulated in Table 3.

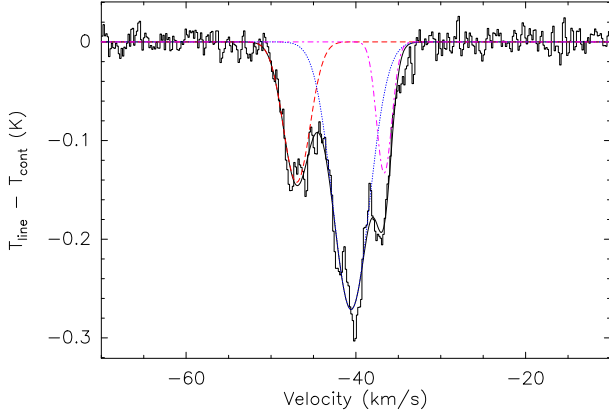


Figure 6. Continuum-subtracted spectrum of $\text{HCO}^+ J=1-0$ at the radio peak of Cas A ($23^{\text{h}}23^{\text{m}}10^{\text{s}}$, $58^{\circ}48'40''$, J2000), fitted with three Gaussian lines. The sum of the three Gaussian components is shown with the black solid line.

picture that Cas A is still expanding within the progenitor’s wind cavity, and the preshock density is low as measured from X-ray observations ($0.9 \pm 0.3 \text{ cm}^{-3}$; Lee et al. 2014).

Table 2. Fit results of the HCO^+ spectrum near the radio peak

V_{LSR} (km s^{-1})	FWHM (km s^{-1})	$T_{\text{line}} - T_{\text{cont}}$ (K)	$N(\text{HCO}^+)^{\text{a}}$ (cm^{-2})
-46.98 ± 0.06	3.7 ± 0.1	-0.14 ± 0.02	1.3×10^{11}
-40.56 ± 0.04	5.1 ± 0.2	-0.27 ± 0.02	3.6×10^{11}
-36.66 ± 0.04	2.1 ± 0.1	-0.13 ± 0.02	7.1×10^{10}

NOTE—The 1σ uncertainty is given.

^aA lower limit of the HCO^+ column density obtained by using $T_{\text{ex}} = 2.73 \text{ K}$ and $T_{\text{cont}} = 4.6 \text{ K}$.

We note that a few regions along the SNR boundary (e.g., regions 5, 7, 13, and 17) show red-shifted ^{12}CO line wings (with widths of a few km s^{-1} ; see Figure 4) of the $V_{\text{LSR}} \sim 47 \text{ km s}^{-1}$ lines. It is difficult, however, to ascribe them to the shock-MC interaction. First, the

MCs in these regions are suggested to be in the foreground of the SNR (see Sections 3.5 and 4.2), which could not account for a disturbance showing a redshifted line feature. Secondly, the small widths of the redshifted wings are not consistent with the ram pressure balance of the cloud shock. The pressure balance can be formulated by $n(\text{H}_2)v(\text{H}_2)^2 \sim n_0v_f^2$ (McKee & Cowie 1975), where $n(\text{H}_2)$ and n_0 are the densities in the cloud and the preshock intercloud medium, respectively, and $v(\text{H}_2)$ and v_f are the velocities of the cloud shock and the blast wave, respectively. For $n_0 \sim 1 \text{ cm}^{-3}$ (Chevalier & Oishi 2003; Lee et al. 2014) and $V_f = 5200 \text{ km s}^{-1}$ (Vink et al. 1998), the cloud shock velocity would be $v(\text{H}_2) \sim 1.6 \times 10^2 [n(\text{H}_2)/10^3 \text{ cm}^{-3}]^{-1/2} \text{ km s}^{-1}$ (MC density $n(\text{H}_2) \sim 10^3 \text{ cm}^{-3}$; Section 4.2). Actually, a molecular line with such a high velocity width is not detected in our observations. A cloud shock with velocity $\gtrsim 50 \text{ km s}^{-1}$ would easily dissociate ambient molecules (e.g., Hollenbach & McKee 1980), but molecules may reform subsequently in post-shock regions and emit broad lines (Hollenbach & McKee 1989; Wallström et al. 2013). Therefore, these wing-like profiles are probably from quiescent MCs along the line of sight with systemic velocities $V_{\text{LSR}} > -47 \text{ km s}^{-1}$.

One should be aware that if the shocked layer is much thinner than the resolution of the telescope, the shocked features might be diluted and difficult to observe. For example, a broadened CO line with $\Delta V = 12 \text{ km s}^{-1}$ was found near SNR Kes 79 with a resolution of $15''$, but such a broad line was not seen under a resolution of $\sim 1'$ (Zhou et al. 2016). In this case, one needs to consider other clues for SNR–MC interaction, such as drastic enhancement of the post-shock density indicated by other wavelengths, which, however, cannot be regarded as direct evidence. Moreover, such clues have not been found in Cas A. Our CO $J=2-1$ observations, with the best angular resolution so far, can resolve a scale of 0.18 pc ($11''$) at the distance of Cas A. According to our observations, the evidence of SNR–MC interaction is lacking.

Although we claim that there is no broad CO emission detected from interstellar MCs toward Cas A, the remnant was found to form CO molecules in the supernova ejecta behind the reverse shock (Rho et al. 2009, 2012), which emit very broad CO emission with ΔV of a few hundred km s^{-1} (Wallström et al. 2013). The velocities of these CO ejecta knots (with V_{LSR} down to -5660 km s^{-1} , Rho et al. 2012) are beyond the velocity range for us to search for shocked interstellar MCs.

4.2. Properties of the foreground MCs

The MCs at $V_{\text{LSR}} = -50$ to -30 km s^{-1} are foreground gas, as suggested by the HCO^+ absorption line (see Sec-

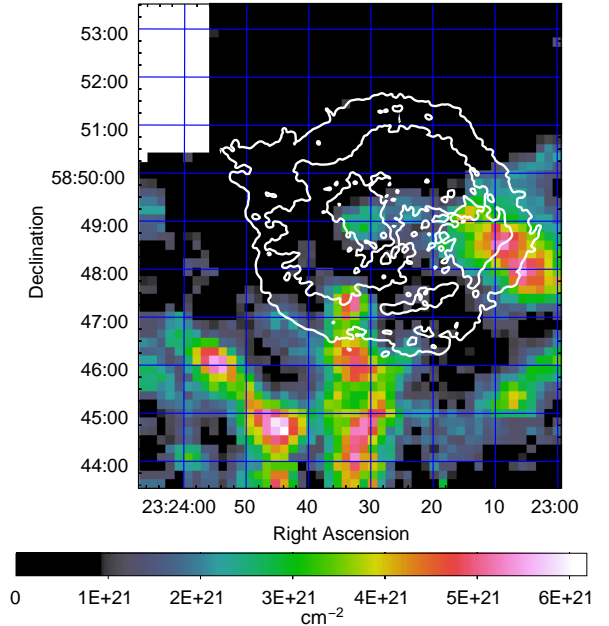


Figure 7. $N(\text{H}_2)$ distribution in the velocity range of -50 to -30 km s^{-1} .

tion 3.5 and Figure 6). We derived the column density $N(\text{H}_2)$ and the molecular mass using ^{13}CO lines, assuming that the lines are optically thin, with $T_k = 20 \text{ K}$ for the MC at -50 to -44 km s^{-1} and $T_k = 13 \text{ K}$ for the MCs at -44 to -30 km s^{-1} . Here we adopt the abundance ratio $[^{13}\text{CO}]/[\text{H}_2]$ of 2×10^{-6} (Dickman 1978). The foreground $N(\text{H}_2)$ distribution at $V_{\text{LSR}} = -50$ to -30 km s^{-1} is shown in Figure 7, with a maximum value of $\sim 6 \times 10^{21} \text{ cm}^{-2}$ in the west and to the southeast of the SNR. The MC component at $V_{\text{LSR}} \sim -2 \text{ km s}^{-1}$ is nearly uniformly distributed, with a mean $N(\text{H}_2)$ of $1.6 \times 10^{20} \text{ cm}^{-2}$ if it has $T_k = 10 \text{ K}$. The total $N(\text{H}_2)$ in the foreground of Cas A is, therefore, the sum of the two components.

The H_2 masses in the FOV are $1040 d_3^2 M_\odot$ and $820 d_3^2 M_\odot$ for the velocity ranges of -50 to -44 km s^{-1} and -44 to -30 km s^{-1} , respectively, where d_3 is the distance of the MCs scaled to 3 kpc . The 20 K warm MCs at $V_{\text{LSR}} = -47 \text{ km s}^{-1}$ contribute an H_2 mass of $\sim 200 d_3^2 M_\odot$ projected onto the SNR. This MC component can explain the detection of the $15\text{--}20 \text{ K}$ dust reservoir of $2\text{--}4 M_\odot$ in front of the remnant (Krause et al. 2004; Dunne et al. 2003; Barlow et al. 2010), given a dust-to-gas mass ratio of ~ 0.01 . On the other hand, the cooler MCs in the velocity range -44 to -30 km s^{-1} contribute an H_2 mass of $\sim 280 d_3^2 M_\odot$ projected onto the SNR.

The mean densities of the MCs are calculated by dividing the column densities by the cloud sizes. At

$V_{\text{LSR}} \sim -47 \text{ km s}^{-1}$, the H_2 column densities at the ^{12}CO emission peaks are $\sim 2\text{--}6 \times 10^{21} \text{ cm}^{-2}$. Given the cloud lengths of parsec scales (see Figure 5), the cloud density is obtained as the order of $n(\text{H}_2) \sim 10^3 \text{ cm}^{-3}$. At -44 to -30 km s^{-1} , the H_2 column densities of the MCs in the SNR west are $< 5 \times 10^{21} \text{ cm}^{-2}$. These clouds sometimes overlap with others along the line of sight, with cloud lengths of parsec scales. Their typical densities are a few times 10^2 cm^{-3} . The H_2 densities estimated here are consistent with the values obtained in the previous CO observation ($\leq 4 \times 10^3 \text{ cm}^{-3}$; Wilson et al. 1993) and the values of $\sim 3 \times 10^2\text{--}10^3 \text{ cm}^{-3}$ from the [CI] and ^{12}CO study (Mookerjee et al. 2006).

4.3. Foreground absorption of Cas A

The high foreground absorption of Cas A is regarded as one reason why the supernova explosion was likely not detected in the seventeenth century (e.g., Reynoso & Goss 2002; Krause et al. 2008). Nevertheless, it is an open question whether the SN was witnessed by Flamsteed in 1680 at sixth magnitude (?). Recently, another possibility was proposed that Cassini might discover the SN in or shortly before 1671 at fourth magnitude (?). The foreground $N(\text{H}_2)$ at the explosion center of Cas A (Thorstensen et al. 2001) is $\sim 2 \times 10^{21} \text{ cm}^{-2}$. It gives a V-band extinction of $A_V \sim 2.0$ by applying an $N_{\text{H}}\text{--}A_V$ conversion factor $N_{\text{H}} = 2.87 \times 10^{21} A_V \text{ cm}^{-2}$ (Foight et al. 2016) and $N_{\text{H}} \approx 2.85 N(\text{H}_2)$ (the value of 2.85 accounts for a photoabsorption cross-section ratio of H_2 to H; Wilms et al. 2000). The extinction contributed by CO-traced molecular gas is smaller than the A_V derived from optical observations ($= 6.2 \pm 0.6$, Eriksen et al. 2009), implying that a lot of foreground materials are in atomic phase or in the form of CO-dark gas (e.g., Oonk et al. 2017; Salas et al. 2018).

The MCs in front of Cas A result in a heavier absorption of the SNR's emission in the west, south, and center (see Figure 7). This is consistent with the fact that larger absorption column densities N_{H} were found in these regions according to spatially resolved X-ray spectroscopy (Yang et al. 2008), the study of OH lines (Keohane et al. 1996), and the extinction map based on *Herschel* observations (De Looze et al. 2017). The largest absorption caused by molecular gas in the west and south is $N_{\text{H}} \approx 2.85 N(\text{H}_2) \sim 1.4 \times 10^{22} \text{ cm}^{-2}$. This N_{H} value is around a half of that in ?, $2.5 \times 10^{22} \text{ cm}^{-2}$, but similar to the result in Yang et al. (2008, $1.5 \times 10^{22} \text{ cm}^{-2}$). The discrepancy of N_{H} in two X-ray studies could be due to the different atomic data or models that they used. The gas in molecular phase likely contributes $\sim 60\%$ of absorption in the west and south of the SNR and $\sim 40\%$ of the absorption near the SNR

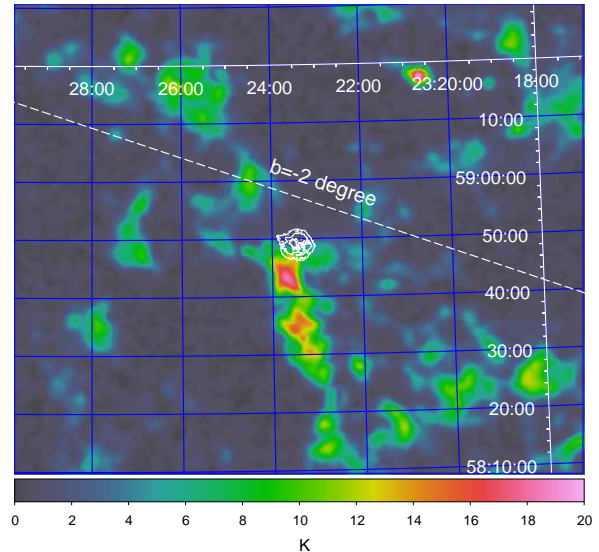


Figure 8. Large-scale FCRAO image of the ^{12}CO $J=1\text{--}0$ main-beam temperature T_{mb} at $V_{\text{LSR}} = -50$ to -44 km s^{-1} .

center, according to a comparison with the N_{H} distribution obtained from the ISM dust (see Figure F3 in De Looze et al. 2017, and the reference of N_{H}/A_V conversion factor therein). Note again that we adopt the abundance ratio $[^{13}\text{CO}]/[\text{H}_2]$ of 2×10^{-6} (Dickman 1978) for calculating $N(\text{H}_2)$.

4.4. The heating source of the warm MC at $\sim 47 \text{ km s}^{-1}$

The CO observation suggests that the SNR suffers from heavier absorption by the MCs in the west, the south and the center, with $N(\text{H}_2)$ up to $5 \times 10^{21} \text{ cm}^{-2}$, $5 \times 10^{21} \text{ cm}^{-2}$, and $2 \times 10^{21} \text{ cm}^{-2}$, respectively.

The foreground MCs at the velocity of -47 km s^{-1} have a temperature of around 20 K, and narrow CO line widths of $1\text{--}3 \text{ km s}^{-1}$ (see Figure 4). The clouds are warmer than those at other velocities (see Figure 3). Figure 8 shows a large-scale image of the ^{12}CO $J=1\text{--}0$ main-beam temperature T_{mb} in the velocity range of -50 to -44 km s^{-1} observed with FCRAO. As indicated by the higher T_{mb} , the warmer gas is along a molecular ridge in the SNR south and extends over $12'$ ($10d_{3.4} \text{ pc}$) south of Cas A.

We here discuss what heating sources cause the elevated temperature of the 20 K clouds. The SNR shocks are not the direct heating source, given that the clouds distribute both inside and far outside of the SNR. Actually, the heating mechanism should be unrelated to any forms of recent turbulences or shocks, since the narrow CO line widths suggest that they are quiescent gas. We can also exclude the progenitor winds of Cas A as the

heating source, as there are no molecular line broadening or systematic shifts of line centers that may result from the winds. The far-UV photons can ionize and heat neutral gas and dissociate molecules; however, they are typically heavily absorbed before reaching deep into the MCs with high column density ($> 10^{21} \text{ cm}^{-2}$). For the far-UV-shielded regions in MCs, the common heating mechanisms are cosmic ray (CR) heating and X-ray heating.

4.4.1. Background CRs

Low-energy CRs ($< 1 \text{ GeV}$) are the main regulators for the ionization and chemical state of dense cores lying deeply inside the far-UV-shielded regions. CR-induced ionization is also accompanied by a heating to the molecular gas, with CR proton heating rate (Goldsmith & Langer 1978)

$$\begin{aligned} \Gamma_{\text{CR}} &= \zeta(\text{H}_2) \Delta Q n(\text{H}_2) \\ &\sim 3.2 \times 10^{-25} \left[\frac{n(\text{H}_2)}{10^3 \text{ cm}^{-3}} \right] \left[\frac{\zeta(\text{H}_2)}{10^{-17} \text{ s}^{-1}} \right] \text{ erg cm}^{-3} \text{ s}^{-1}, \end{aligned} \quad (4)$$

where $\zeta(\text{H}_2)$ is the CR ionization rate of H_2 , and ΔQ is the energy deposited as heat as a result of the heating. A ΔQ of 20 eV is adopted here, but it varies with CR energy (17–26 eV for 10–100 MeV CR protons; Goldsmith & Langer 1978) and gas composition (e.g., 10–20 eV; Glassgold et al. 2012).

The cooling of dense MCs is dominated by molecular lines and dust radiation. For an MC with a density of $\sim 10^3 \text{ cm}^{-3}$, line cooling is approximated by (Goldsmith 2001)

$$\Lambda_{\text{gas}} \sim 6 \times 10^{-24} \left(\frac{T_{\text{k}}}{20 \text{ K}} \right)^{2.4} \left(\frac{dv/dr}{\text{km s}^{-1} \text{ pc}^{-1}} \right) \text{ erg cm}^{-3} \text{ s}^{-1} \quad (5)$$

where dv/dr is the velocity gradient of the clouds, which influences the optical depth $\tau \propto (dv/dr)^{-1}$.

The molecular gas cooling via gas–dust interaction can be expressed as (Tielens 2005)

$$\Lambda_{\text{g-d}} \sim 10^{-27} \left[\frac{n(\text{H}_2)}{10^3 \text{ cm}^{-3}} \right]^2 T_{\text{k}}^{1/2} (T_{\text{k}} - T_{\text{dust}}) \text{ erg cm}^{-3} \text{ s}^{-1} \quad (6)$$

For the 20 K MCs with a density of $\sim 10^3 \text{ cm}^{-3}$, the molecular lines dominate the cooling. Therefore, we solve the kinetic temperature from the thermal equilib-

rium $\Gamma_{\text{CR}} = \Lambda_{\text{gas}}$ for gas with $n(\text{H}_2) = 10^3 \text{ cm}^{-3}$, and obtain

$$T_{\text{k}} \sim 20 \left[\frac{\zeta(\text{H}_2)}{1.9 \times 10^{-16} \text{ s}^{-1}} \right]^{0.42} \left(\frac{dv/dr}{\text{km s}^{-1} \text{ pc}^{-1}} \right)^{-0.42} \text{ K} \quad (7)$$

CRs could heat the MCs to 20 K given an ionization rate $\zeta(\text{H}_2)$ of $\sim 2 \times 10^{-16} \text{ s}^{-1}$ for a typical velocity gradient of $1 \text{ km s}^{-1} \text{ pc}^{-1}$. Neufeld & Wolfire (2017) obtained a CR ionization rate of $2.8 \times 10^{-16} \text{ s}^{-1}$ per H atom for the -47 km s^{-1} clouds toward Cas A, which was an updated value from the measurement given by Oonk et al. (2017, $\geq 2.5 \times 10^{-18} \text{ s}^{-1}$). Our estimated $\zeta(\text{H}_2)$ level is reasonable among the range measured recently in Galactic interstellar MCs (a mean value of $3.5_{-3.0}^{+5.3} \times 10^{-16} \text{ s}^{-1}$; see Indriolo & McCall 2012, and references therein), but larger than the Galactic level suggested in some earlier studies (10^{-17} – 10^{-16} s^{-1} ; e.g., Black & Dalgarno 1977; van der Tak & van Dishoeck 2000).

The different T_{k} values between the -47 km s^{-1} (20 K) and -44 to -30 km s^{-1} (13 K) can be explained even if they are exposed to the same level of $\zeta(\text{H}_2)$. The velocity dispersion of the western MCs at $V_{\text{LSR}} \sim -39 \text{ km s}^{-1}$ is about 3 times of those at $V_{\text{LSR}} \sim -47 \text{ km s}^{-1}$ (see Figure 4), suggesting a larger velocity gradient dv/dr and therefore stronger line cooling at the same density.

4.4.2. CRs from Cas A

Could the CRs of Cas A heat the MCs? Previous observations have shown enhanced CR ionization rate in the MCs close to SNRs W51C ($\sim 10^{-15} \text{ s}^{-1}$; Ceccarelli et al. 2011) and W28 (Vaupré et al. 2014). As CR ionization rate increases with CR energy density, the enhanced $\zeta(\text{H}_2)$ near SNRs is indirect evidence that SNRs can accelerate CR protons. However, it is difficult for the CRs of young SNRs to diffuse very far away from the shock front. The diffusion length of CRs from Cas A over a timescale of t is l_{diff} (see Vink 2012, and references therein) $l_{\text{diff}} = \sqrt{2Dt}$, where the diffusion coefficient $D = \eta Ec / (3eB)$, with η being the deviation from Bohm diffusion. We obtain $l_{\text{diff}} = 2.7 \times 10^{-3} \eta^{1/2} \left(\frac{E}{1 \text{ GeV}} \right)^{1/2} \left(\frac{B}{10 \mu\text{G}} \right)^{-1/2} \left(\frac{t}{340 \text{ yr}} \right)^{1/2} \text{ pc}$. Only the very high energy CRs can reach further from the acceleration site, and very high η (> 100) is required for a diffusion length as high as 10 pc (e.g., 100 TeV CRs can diffuse 8.7 pc way in the medium with $B = 10 \mu\text{G}$ if $\eta = 100$). However, the diffusion coefficients in young SNRs cannot be so large, as indicated by the X-ray synchrotron emission well confined on the SNR shells ($\eta \lesssim 10$, Vink 2012).

For the CRs from Cas A, the proton energy above 10 TeV is $\sim 4.5 \times 10^{47}$ erg, which is calculated using a proton spectrum with a power-law index of -2.2 and an exponential cutoff at 10 TeV and a proton energy of 5.1×10^{48} ergs $^{-1}$ above TeV (Ahnen et al. 2017). These CR protons provide a mean CR energy density near Cas A of $u_{\text{CR}} \sim 4.5 \times 10^{47}$ erg/($4/3\pi l_{\text{diff}}^3$) $\sim 3.7 \times 10^{-12}(l_{\text{diff}}/10 \text{ pc})^{-3}$ erg cm $^{-3}$. The thermal energy density needed by the MCs to raise a temperature of $\Delta T = 10$ K is $\epsilon_{\text{MC}} = 3/2n(\text{H}_2)k\Delta T \sim 2 \times 10^{-12}[n(\text{H}_2)/10^3 \text{ cm}^{-3}]$ erg cm $^{-3}$. If the very high energy CRs from Cas A were the heating sources of the MCs, it would require the CRs to lose half of their energy to MCs, which cannot be true. First, the collision timescale between > 10 TeV CRs and H $_2$ molecules is $\tau_{\text{pp}} = [2n(\text{H}_2)\sigma_{\text{pp}}c]^{-1} \sim 5 \times 10^3$ yr, where $\sigma_{\text{pp}} \sim 10^{-25}$ cm 2 is the cross section for proton-proton collision (TOTEM Collaboration et al. 2011) and $n(\text{H}_2) \sim 10^3$ cm $^{-3}$ is used. This means that the collision chance between the CR protons and nuclei in MCs is low for this 340 yr young SNR. Only a very small fraction of high-energy CR protons can generate proton-proton collision in MCs and initiate cascades of secondary particles. Second, CRs more frequently transfer energy to the MCs through ionization rather than through proton-proton collision. The ionization timescale per CR particle in MCs is estimated to be $\tau_{\text{ion}} = [n(\text{H}_2)\sigma_{\text{ion}}c]^{-1} \gtrsim 77$ yr, where $\sigma_{\text{ion}} < 1.4 \times 10^{-23}$ cm 2 is the ionization cross section for > 10 TeV CR protons (derived from Eq. 31 in Rudd et al. 1985). During the 340 yr, each CR proton may cause no more than 4.4 times of H $_2$ ionization on average while traveling back and forth across the shock front. Each ionization process only takes 37 eV from a CR proton to generate an ion pair (Glassgold et al. 2012). The mean total energy loss per CR proton is $\lesssim 160$ eV, which is negligible in comparison with the CR energy of > 10 TeV. Hence, even if η has an extremely large value of > 1000 to allow the very high energy CRs to diffuse > 10 pc away, the CR energy is still insufficient to heat the MCs.

Therefore, the 20 K MCs at -47 kms $^{-1}$ cannot be heated by CRs from Cas A, but by background CRs.

4.4.3. X-rays from Cas A

Cas A is a bright X-ray source with X-ray luminosity of 3×10^{36} ergs $^{-1}$ in 0.3–10 keV. X-rays can penetrate large column densities of gas ($N_{\text{H}} > 10^{21}$ cm $^{-2}$), photoionize the MCs, and deposit part of the energy to heat the MCs (Maloney et al. 1996). For the X-ray emission with a photon index of 3.28, the X-ray energy heating

rate per volume in 1–10 keV is (Maloney et al. 1996)

$$\Gamma_{\text{X}} \sim 10^{-20} \left(\frac{n_{\text{H}}}{10^3 \text{ cm}^{-3}} \right) \left(\frac{F_{\text{X}}}{\text{erg cm}^{-2} \text{ s}^{-1}} \right) \left(\frac{N_{\text{H}}^{\text{att}}}{10^{22} \text{ cm}^{-2}} \right)^{-2/3} \text{ erg cm}^{-3} \text{ s}^{-1} \quad (8)$$

where n_{H} is the density of H nuclei, F_{X} is the incident X-ray flux in 1–10 keV, and $N_{\text{H}}^{\text{att}}$ is the attenuating column density between the X-ray source and the heated target. The atomic cloud envelope of the MCs contributes a column density $N_{\text{H}} \gtrsim 10^{22}$ cm $^{-3}$ (e.g., Salas et al. 2018), which would have absorbed nearly all soft X-ray photons with energy < 1 keV before the MC center is heated. The fraction of energy transferred to heat is assumed to be 0.3. Here a photon index of 3.28 and a foreground absorption of 1.6×10^{22} cm $^{-2}$ are used to mimic the X-ray spectral shape of Cas A in 0.5–10 keV. This simple model introduces $\sim 20\%$ uncertainties on the X-ray flux, since it does not fit the emission lines in the spectrum.

The youth of Cas A must be taken into account for the X-ray heating and molecular cooling. The cooling timescale of the 20 K cloud is slow, with $\tau_{\text{cool}} = \epsilon_{\text{MC}}/\Gamma_{\text{gas}} \sim 2 \times 10^4$ yr. It means that the MC cooling is not significant during the short lifetime of Cas A and that the thermal equilibrium assumption cannot be used for this case. On the other hand, the timescale of the incident X-ray photons absorbed by the H $_2$ gas is $\tau_{\text{abs}} = [n(\text{H}_2)\sigma_{\text{H}_2}c]^{-1}$, where the photoabsorption cross section of H $_2$ is $\sigma_{\text{H}_2} \sim 2.85\sigma_{\text{H}}$ (Wilms et al. 2000), and $\sigma_{\text{H}}(E) = 2.6 \times 10^{-22}(E/1 \text{ keV})^{-8/3}$ cm 2 according to an empirical fit to the experimental data in 0.5–7 keV (Maloney et al. 1996). For X-ray photons with energies of 1 and 7 keV, we obtain $\tau_{\text{abs}} = 1.4$ yr and 256 yr, respectively. The soft X-ray emission dominates the heating, with an absorption timescale much smaller than the SNR age. Hence, it is only necessary to calculate heating rate based on the required thermal energy.

To raise the MCs' temperature by 10 K (from a typical temperature of 10–20 K), the thermal energy required per volume is $2 \times 10^{-12}[n(\text{H}_2)/10^3 \text{ cm}^{-3}]$ erg cm $^{-3}$. If the thermal energy is constantly provided by the X-ray photons from Cas A during the past 340 yr, the average X-ray heating rate is $\sim 2 \times 10^{-22}[n(\text{H}_2)/10^3 \text{ cm}^{-3}]$ erg cm $^{-3}$ s $^{-1}$. Comparing the value and Equation (8), the required incident X-ray flux at the MCs is obtained as $F_{\text{X}} \sim 10^{-2}(N_{\text{H}}^{\text{att}}/10^{22} \text{ cm}^{-2})^{2/3}$ erg cm $^{-3}$ s. Therefore, it requires the mean X-ray luminosity of Cas A to be $\sim 10^{38}(d_{\text{MC-SNR}}/10 \text{ pc})^2$ ergs $^{-1}$, where $d_{\text{MC-SNR}}$ is the distance between the MC and the SNR, which should be $\gtrsim 10$ pc in order to explain the warm clouds south of Cas A (see also Kantharia et al. 1998; Salas et al. 2017, for the suggestion of a larger distance

of > 100 pc). Since the X-ray luminosity of a young SNR should increase along with the increasing swept-up materials by the shocks, the current X-ray luminosity of Cas A is an upper limit for the SNR's lifetime. Therefore, the required X-ray luminosity is over one order of magnitude larger than the observed X-ray luminosity of Cas A. This suggests that the X-ray emission of Cas A is insufficient to heat the MCs over 10 pc away.

5. CONCLUSION

We have performed mapping observations of $^{12}\text{CO } J=1-0$, $^{12}\text{CO } J=2-1$, $^{13}\text{CO } J=1-0$, and $^{13}\text{CO } J=2-1$ lines and $\text{HCO}^+ J=1-0$ observation toward the SNR Cas A with the IRAM 30 m telescope. Our main conclusions are summarized as follows.

1. ^{12}CO , ^{13}CO , and HCO^+ emission is detected in the velocity range of -50 to -30 km s^{-1} , and at $\sim -2 \text{ km s}^{-1}$. The MCs at $V_{\text{LSR}} = -47 \text{ km s}^{-1}$ have a kinetic temperature of 20 K, narrow line widths of $1-3 \text{ km s}^{-1}$, column densities up to $6 \times 10^{21} \text{ cm}^{-2}$, and density of the order of 10^3 cm^{-3} . Some clouds are distributed in a wide velocity interval of -44 to -30 km s^{-1} , with a mean temperature of 13 K, column density $< 5 \times 10^{21} \text{ cm}^{-2}$, and density of a few $\times 10^2 \text{ cm}^{-3}$.
2. The MCs at $V_{\text{LSR}} = -50$ to -30 km s^{-1} are clumpy. The identified $^{12}\text{CO } J=2-1$ clumps have main-beam temperatures of $2.2 - 16.7$ K, velocity dispersions of $0.3-2.5 \text{ km s}^{-1}$, and sizes from subparsec to 3 pc.
3. The MCs toward Cas A do not show any of the properties that are typical for shocked MCs: (1) optically thin broad line with FWHM much larger than that of the environmental gas, (2) broadened CO lines along with $^{12}\text{CO } J=2-1$ to $J=1-0$ ($R_{21/10} > 1$), and (3) MCs in post-shock regions much hotter than in the preshock regions. Therefore, we suggest that there is no physical evidence to support that the SNR is impacting molecular gas.
4. We detect an absorption line of $\text{HCO}^+ J=1-0$ at $V_{\text{LSR}} = -50$ to -33 km s^{-1} near the radio peak west of the SNR, suggesting that all the detected molecular gas is foreground gas.
5. The foreground MCs result in a high absorption of the SNR emission at the west, south, and center of

the SNR. The 20 K warm gas contributes a foreground mass of $\sim 200d_3^2 M_\odot$ for Cas A, which can explain the cold dust (15–20 K; $2-4 M_\odot$) found in front of Cas A. The cooler MCs in the velocity range -44 to -30 km s^{-1} contribute a foreground H_2 mass of $\sim 280d_3^2 M_\odot$.

6. The gas at $V_{\text{LSR}} \sim -47 \text{ km s}^{-1}$ has a kinetic temperature of 20 K, warmer than MCs at other velocities. The warm gas is extended over 10 pc (projected distance) south of the SNR. CRs are likely the heating source, and the required CR ionization rate is $\zeta(\text{H}_2) \sim 2 \times 10^{-16} \text{ s}^{-1}$. The CRs are provided by the local Galactic CR background, but not by Cas A, since the high-energy CRs from Cas A do not provide enough energy to heat the gas, and its low-energy CRs cannot diffuse far enough to the MCs. The X-ray emission of Cas A is insufficient to heat the MCs.

We are thankful to Claudia Marka for the help on the IRAM observations. We also thank Alex Kraus for providing us with the Effelsberg 32 GHz image of Cas A. P.Z. acknowledges the support from the NWO Veni Fellowship, grant no. 639.041.647 and NSFC grants 11503008 and 11590781. J.-T.L. acknowledges the financial support from NASA through the grants NNX13AE87G, NNH14ZDA001N, and NNX15AM93G. Y.C. acknowledges the support from the 973 Program grants 2017YFA0402600 and 2015CB857100 and NSFC grants 11773014, 11633007, and 11851305. This work is based on observations carried out under project nos. 145-15, 053-16, 136-16, and 029-17 with the IRAM 30 m telescope. IRAM is supported by INSU/CNRS (France), MPG (Germany), and IGN (Spain). The Canadian Galactic Plane Survey (CGPS) is a Canadian project with international partners. The Dominion Radio Astrophysical Observatory is operated as a national facility by the National Research Council of Canada. The Five College Radio Astronomy Observatory CO Survey of the Outer Galaxy was supported by NSF grant AST 94-20159. The CGPS is supported by a grant from the Natural Sciences and Engineering Research Council of Canada.

Software: GILDAS/CLASS (Pety 2005), Starlink (Currie et al. 2014), DS9,³ XSPEC (vers. 12.9.0) (Arnaud 1996).

³ <http://ds9.si.edu/site/Home.html>

REFERENCES

- Ahnen, M. L., Ansoldi, S., Antonelli, L. A., et al. 2017, *MNRAS*, 472, 2956
- Anantharamaiah, K. R., Erickson, W. C., Payne, H. E., & Kantharia, N. G. 1994, *ApJ*, 430, 682
- Arnaud, K. A. 1996, in *Astronomical Society of the Pacific Conference Series*, Vol. 101, *Astronomical Data Analysis Software and Systems V*, ed. G. H. Jacoby & J. Barnes, 17
- Baars, J. W. M., Genzel, R., Pauliny-Toth, I. I. K., & Witzel, A. 1977, *A&A*, 61, 99
- Barlow, M. J., Krause, O., Swinyard, B. M., et al. 2010, *A&A*, 518, L138
- Batrla, W., Walmsley, C. M., & Wilson, T. L. 1984, *A&A*, 136, 127
- Batrla, W., Wilson, T. L., & Martin-Pintado, J. 1983, *A&A*, 119, 139
- Berry, D. S. 2015, *Astronomy and Computing*, 10, 22
- Bieging, J. H., & Crutcher, R. M. 1986, *ApJ*, 310, 853
- Bieging, J. H., Goss, W. M., & Wilcots, E. M. 1991, *ApJS*, 75, 999
- Black, J. H., & Dalgarno, A. 1977, *ApJS*, 34, 405
- Ceccarelli, C., Hily-Blant, P., Montmerle, T., et al. 2011, *ApJL*, 740, L4
- Chevalier, R. A., & Oishi, J. 2003, *ApJL*, 593, L23
- Currie, M. J., Berry, D. S., Jenness, T., et al. 2014, in *Astronomical Society of the Pacific Conference Series*, Vol. 485, *Astronomical Data Analysis Software and Systems XXIII*, ed. N. Manset & P. Forshay, 391
- Dame, T. M., Hartmann, D., & Thaddeus, P. 2001, *ApJ*, 547, 792
- de Jager, G., Graham, D. A., Wielebinski, R., Booth, R. S., & Gruber, G. M. 1978, *A&A*, 64, 17
- De Looze, I., Barlow, M. J., Swinyard, B. M., et al. 2017, *MNRAS*, 465, 3309
- Dickman, R. L. 1978, *ApJS*, 37, 407
- Dunne, L., Eales, S., Ivison, R., Morgan, H., & Edmunds, M. 2003, *Nature*, 424, 285
- Eriksen, K. A., Arnett, D., McCarthy, D. W., & Young, P. 2009, *ApJ*, 697, 29
- Fesen, R. A., Hammell, M. C., Morse, J., et al. 2006, *ApJ*, 645, 283
- Foight, D. R., Güver, T., Özel, F., & Slane, P. O. 2016, *ApJ*, 826, 66
- Glassgold, A. E., Galli, D., & Padovani, M. 2012, *ApJ*, 756, 157
- Godard, B., Falgarone, E., Gerin, M., Hily-Blant, P., & de Luca, M. 2010, *A&A*, 520, A20
- Goldsmith, P. F. 2001, *ApJ*, 557, 736
- Goldsmith, P. F., & Langer, W. D. 1978, *ApJ*, 222, 881
- Goss, W. M., Kalberla, P. M. W., & Dickel, H. R. 1984, *A&A*, 139, 317
- Hacar, A., Alves, J., Burkert, A., & Goldsmith, P. 2016, *A&A*, 591, A104
- Heyer, M. H., Brunt, C., Snell, R. L., et al. 1998, *ApJS*, 115, 241
- Hollenbach, D., & McKee, C. F. 1980, *ApJL*, 241, L47
- . 1989, *ApJ*, 342, 306
- Hwang, U., & Laming, J. M. 2009, *ApJ*, 703, 883
- Indriolo, N., & McCall, B. J. 2012, *ApJ*, 745, 91
- Jiang, B., Chen, Y., Wang, J., et al. 2010, *ApJ*, 712, 1147
- Kantharia, N. G., Anantharamaiah, K. R., & Payne, H. E. 1998, *ApJ*, 506, 758
- Keohane, J. W., Rudnick, L., & Anderson, M. C. 1996, *ApJ*, 466, 309
- Kilpatrick, C. D., Bieging, J. H., & Rieke, G. H. 2014, *ApJ*, 796, 144
- Krause, O., Birkmann, S. M., Rieke, G. H., et al. 2004, *Nature*, 432, 596
- Krause, O., Birkmann, S. M., Usuda, T., et al. 2008, *Science*, 320, 1195
- Laming, J. M., & Hwang, U. 2003, *ApJ*, 597, 347
- Lee, J.-J., Park, S., Hughes, J. P., & Slane, P. O. 2014, *ApJ*, 789, 7
- Lucas, R., & Liszt, H. 1998, *A&A*, 337, 246
- Maloney, P. R., Hollenbach, D. J., & Tielens, A. G. G. M. 1996, *ApJ*, 466, 561
- McKee, C. F., & Cowie, L. L. 1975, *ApJ*, 195, 715
- Mebold, U., & Hills, D. L. 1975, *A&A*, 42, 187
- Mookerjee, B., Kantharia, N. G., Roshni, D. A., & Masur, M. 2006, *MNRAS*, 371, 761
- Neufeld, D. A., & Wolfire, M. G. 2017, *ApJ*, 845, 163
- Oonk, J. B. R., van Weeren, R. J., Salas, P., et al. 2017, *MNRAS*, 465, 1066
- Payne, H. E., Anantharamaiah, K. R., & Erickson, W. C. 1989, *ApJ*, 341, 890
- Pety, J. 2005, in *SF2A-2005: Semaine de l’Astrophysique Française*, ed. F. Casoli, T. Contini, J. M. Hameury, & L. Pagani, 721
- Phillips, T. G., Huggins, P. J., Wannier, P. G., & Scoville, N. Z. 1979, *ApJ*, 231, 720
- Reed, J. E., Hester, J. J., Fabian, A. C., & Winkler, P. F. 1995, *ApJ*, 440, 706
- Reynoso, E. M., & Goss, W. M. 2002, *ApJ*, 575, 871
- Reynoso, E. M., Goss, W. M., Dubner, G. M., Winkler, P. F., & Schwarz, U. J. 1997, *A&A*, 317, 203
- Rho, J., Hewitt, J. W., Boogert, A., Kaufman, M., & Gusdorf, A. 2015, *ApJ*, 812, 44

- Rho, J., Jarrett, T. H., Reach, W. T., Gomez, H., & Andersen, M. 2009, *ApJL*, 693, L39
- Rho, J., Onaka, T., Cami, J., & Reach, W. T. 2012, *ApJL*, 747, L6
- Rudd, M. E., Kim, Y. K., Madison, D. H., & Gallagher, J. W. 1985, *Reviews of Modern Physics*, 57, 965
- Salas, P., Oonk, J. B. R., van Weeren, R. J., et al. 2018, *MNRAS*, 475, 2496
- . 2017, *MNRAS*, 467, 2274
- Schwarz, U. J., Goss, W. M., & Kalberla, P. M. W. 1997, *A&AS*, 123, 43
- Thorstensen, J. R., Fesen, R. A., & van den Bergh, S. 2001, *AJ*, 122, 297
- Tielens, A. G. G. M. 2005, *The Physics and Chemistry of the Interstellar Medium*
- TOTEM Collaboration, Antchev, G., Aspell, P., et al. 2011, *EPL (Europhysics Letters)*, 96, 21002
- van den Bergh, S., Marscher, A. P., & Terzian, Y. 1973, *ApJS*, 26, 19
- van der Tak, F. F. S., & van Dishoeck, E. F. 2000, *A&A*, 358, L79
- van Dishoeck, E. F., Jansen, D. J., & Phillips, T. G. 1993, *A&A*, 279, 541
- Vaupré, S., Hily-Blant, P., Ceccarelli, C., et al. 2014, *A&A*, 568, A50
- Vink, J. 2004, *New Astronomy Review*, 48, 61
- . 2012, *A&A Rv*, 20, 49
- Vink, J., Bloemen, H., Kaastra, J. S., & Bleeker, J. A. M. 1998, *A&A*, 339, 201
- Wallström, S. H. J., Biscaro, C., Salgado, F., et al. 2013, *A&A*, 558, L2
- Willingale, R., et al. 2002, *A&A*, 381, 1039
- Wilms, J., Allen, A., & McCray, R. 2000, *ApJ*, 542, 914
- Wilson, T. L., Mauersberger, R., Muders, D., Przewodnik, A., & Olano, C. A. 1993, *A&A*, 280, 221
- Yang, X., Lu, F., & Chen, L. 2008, *Chinese Journal of Astronomy and Astrophysics*, 8, 439
- Zhou, P., Chen, Y., Safi-Harb, S., et al. 2016, *ApJ*, 831, 192

APPENDIX

A. CLUMP DECOMPOSITION

We apply the FellWalker clumpfind algorithm (Berry 2015) in the STARLINK package to decompose the MCs to clumps. FellWalker is named as an analogy with the British pastime of ascending the hills of north England. It is a watershed algorithm that segments 2D/3D data by identifying the low-lying areas. The maximum value of a clump is at the hill peak, while the pixels on the route uphill but between the watershed and hill peak are assigned to this hill/clump. The minimum number of pixels (three dimensions) in each clump is 16. The detection limit of the clump signal is set to 2 rms (0.7 K).

Table 3 summarizes the detailed information of the identified clumps. The velocity dispersion is given by $dv = (\sum T_i v_i^2 / \sum T_i - (\sum T_i v_i / \sum T_i)^2)^{1/2}$, where T_i is the intensity of the emission at pixel i minus the background value, and v_i is the V_{LSR} of pixel i . For a clump with a Gaussian profile, the dv is equal to the Gaussian standard deviation σ .

Table 3. $^{12}\text{CO } J=2-1$ clumps decomposed from the MCs toward Cas A

clump	R.A.	Decl.	T_{mb}^{P} (K)	V_{LSR} (km s^{-1})	dV (km s^{-1})	clump	R.A.	Decl.	T_{mb}^{P} (K)	V_{LSR} (km s^{-1})	dV (km s^{-1})
c1	23:23:06.4	58:45:16.4	16.7	-47.5	0.9	c40	23:23:08.5	58:50:51.9	7.0	-36.5	1.1
c2	23:23:11.3	58:47:22.9	14.6	-47.5	0.9	c41	23:23:18.4	58:48:39.9	6.8	-35.8	0.6
c3	23:23:51.6	58:45:43.8	14.5	-46.8	0.9	c42	23:23:07.8	58:46:55.4	6.8	-41.0	0.9
c4	23:23:50.2	58:47:22.8	14.4	-46.0	1.3	c43	23:23:21.9	58:46:17.0	6.6	-37.5	0.7
c5	23:23:38.2	58:48: 1.4	14.3	-48.5	1.4	c44	23:23:01.4	58:48:28.8	6.6	-41.2	0.9
c6	23:23:50.9	58:47:39.3	14.1	-47.2	0.9	c45	23:23:00.7	58:48:28.8	6.4	-39.8	0.4
c7	23:23:46.7	58:45:10.9	13.5	-46.2	0.9	c46	23:23:26.2	58:45:11.0	6.4	-36.5	0.5
c8	23:23:11.3	58:48:39.9	13.4	-46.5	0.8	c47	23:23:21.9	58:48:45.5	6.4	-39.5	1.4
c9	23:23:43.1	58:45:32.9	13.1	-46.2	0.9	c48	23:23:19.8	58:45:38.4	6.4	-43.8	1.1
c10	23:23:34.7	58:46: 0.4	12.5	-47.5	1.3	c49	23:23:19.1	58:45:10.9	6.3	-42.5	0.6
c11	23:23:02.8	58:48:50.8	12.1	-47.0	0.9	c50	23:23:53.8	58:46:55.3	6.2	-37.8	0.6
c12	23:23:24.1	58:46:28.0	10.6	-48.5	0.7	c51	23:23:09.2	58:48:39.9	6.1	-41.0	1.0
c13	23:23:32.5	58:45:11.0	10.4	-46.0	0.7	c52	23:23:52.4	58:47: 0.8	6.1	-36.0	0.8
c14	23:23:26.9	58:45:11.0	10.3	-46.0	0.5	c53	23:23:51.7	58:50:29.8	5.9	-35.5	0.7
c15	23:23:21.2	58:48: 1.5	9.8	-47.2	1.2	c54	23:23:45.3	58:47:22.9	5.8	-41.8	0.8
c16	23:23:42.4	58:47:11.9	9.5	-36.8	1.0	c55	23:23:48.1	58:47:44.8	5.5	-36.5	0.6
c17	23:23:13.4	58:47:55.9	8.8	-36.0	2.5	c56	23:23:00.7	58:51:19.3	5.2	-39.8	0.8
c18	23:23:10.6	58:48:39.9	8.7	-37.8	1.4	c57	23:23:48.9	58:50:57.3	5.2	-50.5	0.3
c19	23:23:34.7	58:47: 0.9	8.7	-37.2	0.8	c58	23:23:20.5	58:52: 3.4	5.0	-41.2	0.7
c20	23:23:05.6	58:49:18.3	8.7	-36.2	1.1	c59	23:23:12.7	58:45:10.9	5.0	-36.0	0.5
c21	23:23:19.8	58:47:50.4	8.5	-36.0	0.9	c60	23:23:49.5	58:45:10.8	4.6	-38.0	1.0
c22	23:23:36.1	58:48:45.4	8.5	-44.0	1.1	c61	23:23:22.6	58:50:52.0	4.6	-41.8	0.7
c23	23:23:12.7	58:49:45.9	8.5	-34.8	2.1	c62	23:23:46.7	58:51:41.4	4.3	-36.2	0.9
c24	23:23:14.2	58:46: 0.4	8.0	-47.8	0.7	c63	23:23:46.0	58:48:56.4	4.3	-47.2	0.8
c25	23:23:02.8	58:49:23.8	8.0	-38.8	1.4	c64	23:23:09.2	58:50:46.4	4.3	-40.5	0.7
c26	23:23:03.5	58:50: 7.8	7.6	-41.5	1.0	c65	23:23:53.8	58:51:57.8	4.2	-35.8	0.7
c27	23:23:22.6	58:49:13.0	7.5	-43.5	1.7	c66	23:23:06.4	58:45:54.9	4.0	-37.8	0.6
c28	23:23:34.0	58:49: 7.4	7.4	-39.2	1.4	c67	23:23:10.6	58:45:43.9	4.0	-36.5	0.5
c29	23:23:11.3	58:49:18.4	7.4	-40.0	1.6	c68	23:23:16.3	58:45:10.9	3.9	-37.2	0.6
c30	23:23:07.8	58:45:32.9	7.4	-42.0	1.4	c69	23:23:30.4	58:49:29.5	3.7	-45.8	0.5
c31	23:23:06.4	58:45:27.4	7.4	-44.5	1.0	c70	23:23:12.0	58:50:24.4	3.5	-43.0	0.5
c32	23:23:53.1	58:49: 7.3	7.4	-47.8	0.5	c71	23:23:41.0	58:49:23.9	3.3	-45.5	0.6
c33	23:23:09.9	58:47: 6.4	7.4	-37.8	1.0	c72	23:23:24.1	58:49:13.0	3.3	-36.0	0.5
c34	23:23:39.6	58:48:39.9	7.3	-43.5	1.3	c73	23:23:51.0	58:50:13.3	3.2	-38.2	0.5
c35	23:23:08.5	58:47: 0.9	7.3	-36.2	0.7	c74	23:23:03.5	58:51:52.3	2.8	-37.0	0.5
c36	23:23:23.3	58:45:11.0	7.3	-41.5	1.1	c75	23:23:53.8	58:46: 0.3	2.7	-42.8	0.5
c37	23:23:26.9	58:45:16.5	7.2	-38.0	0.7	c76	23:23:29.0	58:48:51.0	2.6	-48.5	0.5
c38	23:23:37.5	58:48:23.4	7.2	-35.0	0.8	c77	23:23:53.8	58:45:54.8	2.3	-42.2	0.4
c39	23:23:16.3	58:48:28.9	7.2	-37.5	0.8	c78	23:23:00.6	58:51:30.3	2.2	-35.0	0.3

NOTE—For each clump, the coordinates and V_{LSR} are given for the pixel with peak $^{12}\text{CO } J=2-1$ intensity T_{mb}^{P} , and dv is the velocity dispersion of the clump.